Preparation for ApJ

Discovery of Extremely Embedded X-ray Sources in the R Coronae Australis Star Forming Core

Kenji Hamaguchi[1], Michael F. Corcoran[2], Rob Petre, Nicholas E. White

Laboratory for High Energy Astrophysics, Goddard Space Flight Center, Greenbelt, MD 20771, USA

kenji@milkyway.gsfc.nasa.gov

and

Beate Stelzer

INAF, Osservatorio Astronomico di Palermo, Piazza del Parlamento 1, I-90134 Palermo, Italy

and

Ko Nedachi, Naoto Kobayashi

University of Tokyo, Japan

ABSTRACT

We detected three extremely embedded X-ray sources in the R Corona Australis (R CrA) star forming core, IRS 7 region. Two weak X-ray sources are associated with the VLA centimeter radio sources 10E & W, whereas the third brightest source detected in the two *XMM-Newton* observations on March 2003 has no counterpart at any wavelengths. The large K-band upper-limit (19.4^{m}) measured with the University of Hawaii 88-inch Telescope and strong absorption derived in X-rays ($N_{\rm H}$ $\sim$$2.8\times10^{23}$ cm^{-2} equivalent to $A_{\rm V}$ $\sim$$180^{m}$) indicate that the source is younger than typical Class I protostars, i.e. a Class 0 protostar or an intermittent phase between Class 0 and Class I protostars. The X-ray luminosity was less than one thirtieth ($\log L_{\rm X}$ $\lesssim$29.3 ergs s^{-1}) in the former *Chandra*

[1]National Research Council, 500 Fifth Street, NW, Washington, DC 20001, USA

[2]Universities Space Research Association, 7501 Forbes Blvd, Ste 206, Seabrook, MD 20706, USA

observation in October 2000, which suggests that the X-ray activity, probably generated by magnetic activity, is triggered by an intermittent mass accretion episode such as FU Ori type outbursts. Because the source was detected at high significance in the *XMM-Newton* observations (∼2,000 cnts), X-ray properties of such young protostars can be well investigated for the first time. The light curves were constant in the 1st observation and increased linearly by a factor of two during 30 ksec in the 2nd observation. Both spectra showed iron K lines originated in hot thin-thermal plasma and fluorescence by cold gas. They can be reproduced by an absorbed thin-thermal plasma model with a Gaussian component at 6.4 keV (kT ∼3−4 keV, $L_{\rm X}$ ∼7−20×10^{30} ergs s^{-1}). The rising timescale of the light curves in the 2nd observation was too slow for magnetically generated X-ray flares, whereas large equivalent width of the fluorescence iron K line in the 1st observation (∼810 eV) requires strong partial covering of the X-ray source. These results suggest that a confined hot (perhaps accretion) spot on the proto-stellar core was behind the star in the 1st observation and just appeared in the 2nd observation due to the core rotation with period of $\gtrsim$2.8 days, which is much slower than the break-up velocity previously assumed for young protostars. This means that the source had quiescent X-ray activity during the observations with an order of magnitude stronger level than Class I (older) protostars. We also consider whether the X-ray source associated with 10E could be shock heated plasma by a collision of a jet emanating from the tentative Class 0 object.

Subject headings: stars: activity — stars: pre–main-sequence — X-rays: stars

1. Introduction

The youngest phase of solar type stars, low mass protostars, are found deep inside molecular cloud cores. Violent mass accretion is believed to occur onto the proto-stellar core, but the activity is generally hidden inside an enormous thickness of gas. From spectral energy distribution (SED) in the infrared (IR) and radio wavelengths, protostars are divided into two classes, which are thought to represent their evolutionary status. The former phase of protostars designated as Class 0 objects (∼10^4-year-old) mainly have far-IR and submillimeter emission from cold circumstellar dust (T <30 K, Andre et al. 1993). They are thought to undergo dynamical mass accretion from huge circumstellar envelopes. The latter phase of protostars designated as Class I objects (∼10^5-year-old) can be observed in the near-IR wavelength. The proto-stellar cores become hot (T ∼3000−5000 K) by assembling most of their stellar mass (late accretion phase).

X-ray observations, especially in the hard X-ray band transparent for thick molecular clouds, have shown high energy activity on Class I objects (Koyama et al. 1996; Grosso et al. 1997; Imanishi et al. 2001). The X-ray activity is probably driven by magnetic activity close to the proto-stellar core as is suggested by occasional rapid X-ray flares reminiscent of solar flares. A solar-type magnetic dynamo does not work on protostars according to current theories. As an alternative mechanism, reconnection of fossil magnetic fields linked to the mass accretion process has been proposed (Koyama et al. 1996; Montmerle et al. 2000).

X-ray emission from extremely embedded sources ($N_{\rm H}$ $\sim$1$-$3$\times10^{23}$cm^{-2}) was first reported in the OMC-2/3 cloud (Tsuboi et al. 2001). They have characteristics of Class 0 object as having no near-IR counterparts and associating with millimeter radio clumps. However, follow-up radio and near-IR observations by Tsujimoto et al. (2004) did not classify them as Class 0 protostars unambiguously. In particular, one of the two candidates have good correlation with a centimeter radio source and a jet feature in the H_2 band, evidence for excitation by a jet ejected from a nearby Class I protostar. Furthermore, X-ray photons obtained in the observation ($\approx$50 photons) was too small to deduce reliable plasma parameters or variability. Though there is also other X-ray detections from cores associated with Class 0 candidates in the Trifid nebula (Rho et al. 2004), long distance to the sources (d $\sim$1.7 kpc) makes their identification far more difficult. To date no X-ray sources has been identified with a bona-fide Class 0 object.

The R Corona Australis (R CrA) cloud is a nearby low and intermediate-mass star forming region (d $\sim$170 pc, Knude & Hϕg 1998). Among many young stellar objects in the cloud, those in the IRS 7 region have attracted particular interest as a cite of ongoing star formation. The region contains double peaked strong centimeter emission; one in the east designated as 10E (or IRS 7B) and the other in the west designated as 10W (IRS 7A) (Brown 1987; Feigelson et al. 1998; Harju et al. 2001). It also has corresponding two submillimeter peaks (van den Ancker 1999), multiple millimeter continuum peaks (Henning et al. 1994; Saraceno et al. 1996; Chini et al. 2003; Choi & Tatematsu 2004) and signature of strong bipolar outflows (Harju et al. 1993; Anderson et al. 1997), whereas it has only one near-IR source associated with 10W (Wilking et al. 1997). These characteristics make the IRS 7 region a promising host of Class 0 sources. Koyama et al. (1996) detected hard X-ray emission and an intense flare from the IRS 7 region, possibly from IRS 7 (R1), suggesting a protostar with high energy (magnetic) activity.

In this paper, we report on the X-ray detection of extremely embedded sources in the IRS 7 star forming core during *XMM-Newton* observations in 2003. These results combined with analyses of an earlier *Chandra* observation in 2001 and follow-up near-IR observations with the University of Hawaii 88-inch Telescope (UH88) help to understand the nature of

the detected X-ray sources.

2. X-ray Observations and Absolute Position Correction

We analyzed the X-ray data obtained with the *XMM-Newton* observatory in two observations on 2003 March 28 (hereafter $\mathrm{Obs_{XMM1}}$) and March 29 ($\mathrm{Obs_{XMM2}}$) (Table 1). The *XMM-Newton* satellite (Jansen et al. 2001) has three nested Wolter I type X-ray telescopes (Aschenbach et al. 2000) with two types of CCD cameras (one EPIC-pn camera and two EPIC MOS cameras, Strüder et al. 2001; Turner et al. 2001) on their focal planes. During the observations, all CCD cameras were operated in full frame mode with the medium filter inserted. $\mathrm{Obs_{XMM1}}$ and $\mathrm{Obs_{XMM2}}$ had the same satellite pointings. The IRS 7 star forming core was at 6′ off-axis, where the 90% photon radius is $\sim$1′. The analysis was performed with the software package SAS ver. 5.4.1 and LHEASOFT ver. 5.2. The observing data were processed using the SAS scripts "emchain" and "epchain". Events detected during pn frame transfer, called "out of time events", were reproduced as well. Events with pattern $\leqq$12 (pattern $\leqq$4 for pn spectral analysis) were selected. High background periods, defined as count rate of "pattern = 0" events above 10 keV across the entire chip above 0.35 cnts $\mathrm{s^{-1}}$ for MOS and 1 cnts $\mathrm{s^{-1}}$ for pn, were screened out. Events close to hot pixels or outside the field of view (FLAG = 0) were also removed.

To help source identification and investigate long-term flux variations, we analyzed the archival *Chandra* observation on 2000 October 7 (hereafter $\mathrm{Obs_{CXO}}$, Table 1), whose first result was presented by Garmire & Garmire (2002). *Chandra* has one X-ray telescope with capability of sub-arcsecond imaging and two inter-changeable detectors (Weisskopf et al. 2002). In the observation, the ACIS-I CCD camera arrays were selected. The IRS 7 star forming region was at 2′ off-axis, where the 90% photon radius is $\sim$1.″3. The analysis was performed with the software package CIAO ver. 2.3 and LHEASOFT ver. 5.2. The level 1 event data were reprocessed with "acis_process_events" to compensate for degradation of the CCD spectral resolution by charge transfer inefficiency (CTI, Townsley et al. 2000). Events with grade 0, 2, 3, 4 and 6 were selected.

For correction of absolute coordinates, positions of nine X-ray bright sources (two more sources for the *Chandra* data) on the EPIC pn plus MOS image (0.3−10 keV) and the ACIS-I image (0.5−9 keV) were measured using source detection packages (SAS: *edetect_chain*, CIAO: *wavdetect*). These positions are correlated with 2μm IR sources in the 2MASS All-Sky Point Source Catalog (PSC) obtained from NASA/IPAC Infrared Science

Archive (GATOR)[1]. The astrometric accuracy of this catalogue is good around 0.″ 1[2]. Each X-ray source has only one 2MASS counterpart within 4″, so that source misidentification is not a problem. After adjusting the X-ray data frames as shown in Table 1, deviation of *Chandra* and *XMM-Newton* coordinates from the 2MASS frame is $\lesssim$ 0.″ 6.

3. X-ray Image

During the *XMM-Newton* observations, strong hard X-ray emission was detected from the IRS 7 star forming core. Figure 1 shows the true color EPIC pn + MOS image of the R CrA star forming region combining the $\mathrm{Obs_{XMM1}}$ and $\mathrm{Obs_{XMM2}}$ data. The image is color-coded to represent soft band (0.2–1 keV) to red, medium band (1–3 keV) to green and hard band (3–9 keV) to blue. The IRS 7 region has darker blue than the other Class I candidates, suggesting that the emission is heavily absorbed. The left panel of Figure 2 magnifies the IRS 7 region of the blue band (3–9 keV) image, shown in black and white. A strong X-ray source ($\mathrm{X_E^{XMM}}$) was detected near the radio source 10E in both $\mathrm{Obs_{XMM1}}$ and $\mathrm{Obs_{XMM2}}$ (Table 2). The coordinates derived from each observation with *edetect_chain* are consistent ($\lesssim$0.″ 3 discrepancy) so that the sources seen in $\mathrm{Obs_{XMM1}}$ and $\mathrm{Obs_{XMM2}}$ would be identical. We also found another faint X-ray source ($\mathrm{X_W^{XMM}}$, $\sim 14\sigma$ significance for the $\mathrm{Obs_{XMM1}}$ data) to the north-east direction of $\mathrm{X_E^{XMM}}$. The source was not detected with *edetect_chain* probably due to crowdedness of the region.

Chandra detected two weak X-ray sources in the IRS 7 region at above 6σ significance ($\mathrm{X_E^{CXO}}$ and $\mathrm{X_W^{CXO}}$, see Table 2 and the top right panel of Figure 2). $\mathrm{X_W^{CXO}}$ is identified with $\mathrm{X_W^{XMM}}$ (hereafter we call it $\mathrm{X_W}$), but $\mathrm{X_E^{CXO}}$ has a 2″ offset to south-east from $\mathrm{X_E^{XMM}}$ although position accuracy of $\mathrm{X_E^{XMM}}$ could have additional unknown uncertainty affected by unresolved sources. This suggests no X-ray emission from $\mathrm{X_E^{XMM}}$ detected in $\mathrm{Obs_{CXO}}$, while $\mathrm{X_E^{CXO}}$ emission in $\mathrm{Obs_{XMM1}}$ and $\mathrm{Obs_{XMM2}}$, if present, can be obscured by the wings of $\mathrm{X_E^{XMM}}$ point-spread-function. (We think that the component of $\mathrm{X_E^{CXO}}$ is marginally resolved in the spectra of $\mathrm{X_E^{XMM}}$, see section 4.1).

Compared with field sources in the other wavelengths (the bottom right panel of Figure 2), $\mathrm{X_W}$ has VLA centimeter (10W in Brown 1987), millimeter (source 4 in Choi & Tatematsu 2004) radio, and near-IR (IRS 7) counterparts. $\mathrm{X_E^{CXO}}$ has a VLA centimeter (10E in Brown 1987) radio counterpart. $\mathrm{X_E^{XMM}}$ has no counterpart in any other wavelength.

---

[1]http://irsa.ipac.caltech.edu/applications/Gator/

[2]Sect. 2.2 of Explanatory Supplement to the 2MASS All-Sky Data Release: http://www.ipac.caltech.edu/2mass/releases/allsky/doc/

4. X-ray Light Curves and Spectra

With ∼2,000 X-ray events obtained from X_E^{XMM} with *XMM-Newton*, we could perform detailed timing and spectral analysis. Photon statistics events of the other sources are quite limited (10−120 photons). We briefly show their spectral analyses.

4.1. East Sources (X_E^{XMM} & X_E^{CXO})

Source events of X_E^{XMM} were extracted from a 27.″ 5 radius circle centered on the source position excluding the region around X_W^{XMM} (like a crescent shape). Background was selected from source free regions. Source events from X_E^{CXO} were extracted from a 1.″ 8 radius circle centered on the source position. The background has a negligible contamination.

Plots in the top panel of Figure 3 show background subtracted light curves of X_E^{XMM} in the 2−10 keV band. The light curves in Obs_{XMM1} (first half) were rather flat with marginal fluctuation in the latter observation. A constant model in a χ^2 fit is acceptable at the 90% confidence (Table 3). Count rates in Obs_{XMM2} started at around four times as high as the average count rate in Obs_{XMM1}. The light curves gradually increased by a factor of two throughout Obs_{XMM2} except for two dips at around 8.02 and 8.17 days. They are consistent with a linear model with a slope of $\sim 9.3 \times 10^{-2}$ cnts s^{-1} day^{-1}. The hardness ratio defined as count rates in the 5−10 keV band over those in the 2−5 keV band (bottom panel of Figure 3) remained unchanged within statistics both in Obs_{XMM1} and Obs_{XMM2} except for a strange minimum at 7.86 day. This means that time variation is not accompanied by significant change of the spectral shape. On the other hand, the X-ray dips on timescales of <1 ksec are unusual, but they do not seem to be artificial: both pn and MOS light curves without background subtraction also show such dips; other nearby sources (R CrA, IRS 5 and CrA 1) have no dips at those timings; similar dips are seen at 7.85 (only MOS data shown with diamonds in Figure 3 is available) and 6.56 days with less significance (see arrows in Figure 3). Interestingly, these dips are on a period of ∼13.9 ksec with the exception of the dip at 6.40 days which is missing.

The spectra of X_E^{XMM} in Obs_{XMM1} and Obs_{XMM2} (Figure 4) show several similarities. X-ray emission in both reaches up to ∼10 keV and is strongly absorbed below 2−3 keV. It has a broad line feature between 6−7 keV, and marginal lines, which are not obvious in the EPIC MOS spectra, between 5−6 keV. Origin of the marginal line feature is a puzzle because there is no emission line of any abundant element between 5−6 keV, whereas the

background chromium line of the EPIC pn at 5.5 keV[3] is too weak to show such a feature. To investigate the line feature between 6–7 keV, we tentatively tried a simultaneous fit of the pn and MOS spectra of $\mathrm{Obs_{XMM2}}$ by an absorbed power-law model with a Gaussian component. An acceptable fit at above 90% confidence has the photon index of 3.0 (2.5–3.4), the Gaussian center energy of 6.60 (6.53–6.67) keV and the Gaussian sigma of 0.15 (0.079–0.28) keV (braces show 90% confidence range). Taking into account the source as a promising young stellar origin (see discussion 6.1), the significant line broadening is reasonably regarded as a blend of line emission from He-like iron in hot plasma (∼6.7 keV) and neutral (fluorescent) iron (∼6.4 keV) in cold gas rather than a Doppler broadening with Δv ∼7,000 km $\mathrm{s^{-1}}$. We therefore simultaneously fit both pn and MOS spectra for each observation by an absorbed 1-temperature (1T) thin-thermal plasma model (absorption: Morrison & McCammon 1983, emission: the MeKaL plasma code, Mewe et al. 1995) with a Gaussian component with the fixed line center at 6.4 keV. Fits for each observation are acceptable above 90% confidence (Table 4, Model A and B for $\mathrm{Obs_{XMM1}}$ and $\mathrm{Obs_{XMM2}}$, respectively), but N_{H} has significant discrepancy between $\mathrm{Obs_{XMM1}}$ and $\mathrm{Obs_{XMM2}}$. N_{H} for $\mathrm{Obs_{XMM1}}$ is determined from the slope between 1−5 keV, whereas that for $\mathrm{Obs_{XMM2}}$ is from the steep slope around 3−5 keV, neglecting weak emission below 3 keV. Considering that emission below 3 keV seems unchanged between $\mathrm{Obs_{XMM1}}$ and $\mathrm{Obs_{XMM2}}$ in Figure 4, we believe that a model with soft constant emission below 3 keV and hard variable emission above is more realistic. We thus refit the spectra of $\mathrm{Obs_{XMM1}}$ and $\mathrm{Obs_{XMM2}}$ simultaneously by an absorbed 2T model with a Gaussian component at 6.4 keV. In the model, a 1T component for the soft constant emission, N_{H} of the hard variable component and elemental abundance for both components were tied together between $\mathrm{Obs_{XMM1}}$ and $\mathrm{Obs_{XMM2}}$. Whereas, N_{H} parameters of the constant and variable components were independently varied because a model with a common N_{H} gives unrealistically large absorption corrected X-ray luminosity for the constant component as a stellar origin ($\log L_{\mathrm{X}} \sim 35$ ergs $\mathrm{s^{-1}}$). The model (Model C in Table 4), again, successfully reproduced the spectra at above 90% confidence. The absorption column in the best-fit model is extremely large $\sim 2.8 \times 10^{23}$ $\mathrm{cm^{-2}}$, equivalent to $A_{\mathrm{V}} \sim 180^{m}$ (Imanishi et al. 2001). Plasma temperature is ∼2.7 keV in $\mathrm{Obs_{XMM1}}$ and rises to ∼4.0 keV in $\mathrm{Obs_{XMM2}}$. The absorption corrected X-ray luminosity in $\mathrm{Obs_{XMM1}}$ ($\log L_{\mathrm{X}}$ ∼30.8 ergs $\mathrm{s^{-1}}$) is large, which further increases in $\mathrm{Obs_{XMM2}}$ to $\log L_{\mathrm{X}}$ ∼31.2 ergs $\mathrm{s^{-1}}$. Metal abundance is sub-solar (∼0.2 solar), which is typical of low mass young stars. The fluorescent iron line has equivalent width (EW) of ∼810 (240−1400) eV in $\mathrm{Obs_{XMM1}}$, which is one of the largest among young stellar origin (e.g. Imanishi et al. 2001). The line intensity did not change significantly in $\mathrm{Obs_{XMM2}}$, and therefore EW dropped to ∼250 (100−400) eV (braces show 90% confidence

[3]Sect. 3.3.7.2 in *XMM-Newton* Users Handbook,
http://xmm.vilspa.esa.es/external/xmm_user_support/documentation/uhb/index.html

range).

The X-ray spectrum of X_E^{CXO} (left panel of Figure 5) looks rather flat between 1−10 keV though its statistics is poor (∼20 photons). The shape is, roughly speaking, not like the hard variable component of X_E^{XMM}, which has deep absorption below 3 keV, but like the soft constant component. Indeed, X_E^{CXO} has 3 cnts below 3 keV, whose 99% confidence range is between 0.39 cnts and 10.15 cnts ($N = 3$, $B = 0$ in Table 3 of Kraft et al. 1991). If X_E^{CXO} were identical to the hard variable component of X_E^{XMM}, the normalized photon counts below 3 keV should amount to only ∼0.18 cnts. Remembering that X_E^{CXO} has a 2″ offset from X_E^{XMM} (see section 3) and is included in the source region of X_E^{XMM}, it would be identical to the minor (=soft constant) component of X_E^{XMM}. We modeled the spectrum of X_E^{CXO} by an absorbed 1T model fixing N_H at 4.2×10^{22} cm^{-2}, the best-fit value of the soft constant component, and varying kT. An acceptable model (Model D in Table 4) has hot plasma temperature >4 keV and an X-ray flux of one third of the soft constant component of X_E^{XMM}.

During Obs_{CXO}, no X-ray photon was detected within the error circle of X_E^{XMM} (see Figure 2), suggesting that the hard variable component of X_E^{XMM} was below the detection level (<3 photons at the 95% confidence referring to $N = 0$, $B = 0$ in Table 2 of Kraft et al. 1991). Assuming kT ∼3 keV and N_H ∼2.8×10^{23} cm^{-2}, the X-ray luminosity is log $L_X \lesssim$29.3 ergs s^{-1}, which is ∼1/30 of the hard variable component in Obs_{XMM1}. It might be in an inactive (dormant) phase during Obs_{CXO}.

4.2. West Source (X_W)

Source events of X_W^{XMM} (X_W during Obs_{XMM1} and Obs_{XMM2}) were extracted from an ellipse with 15″ long and 10.″5 short axes elongated toward the NNE direction, excluding a region with strong contamination from X_E^{XMM}. The background events are extracted from a symmetrical region of the source region with respect to X_E^{XMM}. The Obs_{XMM2} data were not used due to stronger contamination from X_E^{XMM}. Source events of X_W^{CXO} (X_W during Obs_{CXO}) were extracted from a 1.″8 radius circle. The background has a negligible contamination.

EPIC pn and MOS spectra of X_W^{XMM} (right panel of Figure 5) were reproduced by an absorbed 1T model with strong absorption (N_H ∼3.4×10^{23} cm^{-2}), hot plasma temperature (kT >1.6 keV) and log L_X ∼ 30.5 ergs s^{-1} (Model E in Table 4). Because photon counts of X_W^{CXO} was quite poor (∼13 photons), it is reproduced by the best-fit model of X_W^{XMM} just by changing its normalization (Model F in Table 4). The X-ray luminosity (log L_X ∼ 30.0 ergs s^{-1}) is around one third of that during Obs_{XMM1}.

5. Follow-up Observation in the Near-IR

Infrared source catalogues currently available have several shortcomings for our study: shallow limiting magnitude (e.g. $K_{limit} \sim 15^m$ for 2MASS, 16.5^m for Wilking et al. 1997); too large pixel scales to resolve objects from nearby nebulosity (e.g. $1''$ pix^{-1} for 2MASS and $0.''75$ pix^{-1} for Wilking et al. 1997); insufficient positional accuracy (e.g., $\pm 1''$ for Wilking et al. 1997). We therefore analyzed two deep K-band images of the field obtained in August 1998 and August 2003 using UH88 and the near-infrared imager QUIRC. (Full analysis of the data covering $\sim 100'$ *fov* will be published elsewhere.) During the observations, the f/10 secondary mirror was used, yielding the pixel scale of $0.''1886$ pix^{-1}. The spatial resolution of our images are $0.''5$ and $0.''8$ in FWHM for the data of 1998 and 2003, respectively. The analysis was made with IRAF[4].

Both images were set to the absolute coordinate by referring to the coordinate of R CrA in the 2MASS catalogue. Since the positions of R CrA in the UH88 frames were difficult to measure because of saturation, we measured the positions of IRS 9 and derived the relation between R CrA and IRS 9 from a high resolution image ($0.''14$) obtained with the SUBARU $8.2m$ telescope with the adaptive optics system (Nedachi et al. in preparation). The final positional errors of our images are estimated at $\sim 0.''3$ at maximum. Both images look the same except for their data quality. The top left panel of Figure 6 shows the image taken in 1998 in better condition. In the image, we see filamentary and mildly extended reflection nebulae of R CrA. To highlight fine structures smaller than $10''$ scales for aiding source detection, we median-filtered the image with a $10'' \times 10''$ box and subtracted the resulting image (the bottom panel of Figure 6) from the original. The result is shown in the top right panel of Figure 6. We found no significant emission from X_E^{XMM} and X_E^{CXO} though we see a marginal enhancement of flux at the location of X_E^{CXO}. To determine their flux upperlimit, we flattened the background (mainly extended nebular emission of R CrA) by subtracting the fitted third-order polynomial surfaces from the original images, and measured fluctuation of a subset of the image containing 20×20 pixels at that location of the sources. The 5-σ detection upperlimit for both sources at 50% flux enclosure radius were $\sim 19.4^m$ for the 1998 image and $\sim 19^m$ for the 2003 image. The absolute coordinate of IRS 7 measured with the SUBARU image (Nedachi et al. in preparation) is determined at (α_{2000}, δ_{2000}) = (19h1m55.34s, −36d57'21.69") within $0.''3$ accuracy. With our new coordinate, IRS 7 falls in the potitional error circle of X_E^{CXO}, as shown in Figure 2.

---

[4]IRAF is distributed by the National Optical Astronomy Observatories, which are operated by the Association of Universities for Research in Astronomy, Inc., under cooperative agreement with the National Science Foundation.

6. Discussion

6.1. The Nature and X-ray Emission Mechanism of X_E^{XMM}

X_E^{XMM} has no known IR nor radio counterpart. It could be a background AGN serendipitously discovered. However, AGNs above the observed X-ray flux ($2-8 \times 10^{-13}$ ergs cm^{-2} s^{-1} between 2−10 keV) are found $\lesssim$10 degree $^{-2}$ in the sky (Ueda et al. 1998), and the probability to detect such an AGN in the IRS 7 star forming core ($\sim$10arcsec^2) is extremely small ($\lesssim 10^{-4}$). Furthermore, the spectra show thermal iron K emission line unusual for an AGN and, if we try to fit the X-ray spectrum in Obs_{XMM2} by an absorbed power law model, its spectral photon index of $\sim$3.0 is far larger than the AGN standard ($\Gamma \leq 2$ for AGNs, Ueda et al. 1998). These facts exclude an AGN origin. Taking its location into account, X_E^{XMM} is most likely an unknown very young stellar object.

The large X-ray absorption column ($N_H \sim 2.8 \times 10^{23}$ cm^{-2}) and small near-IR luminosity ($K \gtrsim 19.4^m$) compared with nearby Class I objects such as IRS 1, 2 and 5 ($N_H \sim 2 \times 10^{22}$ cm^{-2}: our additional analysis of the *XMM-Newton* data, $K \lesssim 11^m$: Wilking et al. 1997) mean that X_E^{XMM} has a huge circumstellar envelope which has not well heated up yet. Certainly, van den Ancker (1999) indicated a strong submillimeter (450 &850 μm) condensation around X_E^{XMM}. This strongly suggests that X_E^{XMM} is much younger than typical Class I objects, that is, it is a Class 0 object or an intermediate phase between Class 0 and I objects (hereafter we call it "young protostars"). We should note that the X-ray absorption column is as same as those of the Class 0 candidates in the OMC 2/3 cloud ($N_H \sim 1-3 \times 10^{23}$ cm^{-2}, Tsuboi et al. 2001).

X_E^{XMM} was less X-ray luminous during Obs_{CXO} ($\lesssim$1/30 of Obs_{XMM1}). Though photon statistics are poor, the source looks similarly in activity in another *XMM-Newton* observation on April 2001. This suggests that the X-ray activity was dramatically enhanced during Obs_{XMM1} and Obs_{XMM2}. Such X-ray variation on long time scales is seen in young stars with FU Ori type mass accretion outbursts (Kastner et al. 2004). The X-ray activity during Obs_{XMM1} and Obs_{XMM2} might relate to a mass accretion episode.

The slow linear flux increase by a factor of two during $\sim$30 ksec in Obs_{XMM2} is unlike magnetically driven X-ray flares in young stellar objects and the Sun, both of which are characterized by rapid flux increases within 10 ksec (e.g. Tsuboi et al. 1998, 2000; Stelzer et al. 2000; Imanishi et al. 2001). Favata et al. (2003) found a similar event (a factor of 4 increase during 50 ksec) on the classical T-Tauri star XZ Tau. The event accompanied N_H decrease as the flux increase so that Favata et al. (2003) interpreted it as eclipsing of the emitting region by the accretion stream. We did not find significant variation of spectral shape in the hardness ratio of X_E^{XMM} (Figure 3). Therefore this model would at least need

some modification to apply to X_E^{XMM} such as partial covering by an optically thick absorber with $N_H \gtrsim 10^{24}$ cm^{-2}.

Fluorescent iron lines have been rarely observed in stellar X-ray emission. Even a few examples during strong flares from Class I sources have EW$\lesssim$ 150 eV (Imanishi et al. 2001). Large EW of X_E^{XMM} again suggests it to be extremely embedded in the molecular cloud and/or to have very hot plasma (kT ~4 keV). Inoue (1985) made a simulation of EW of fluorescent iron line assuming possible geometries of surrounding gas (disk + envelope), a power law spectrum of $\Gamma \sim 1.1$ and 1 solar iron abundance for the surrounding matter. To apply the result to X_E^{XMM}, EW shown in Figure 4 of Inoue (1985) should be reduced to ~60% for Obs_{XMM1} and ~80% for Obs_{XMM2} because thermal emission of kT ~2.7 keV and 4 keV has ~40 and 20% lower X-ray flux around the iron K edge energy (7–9 keV) against continuum flux at iron fluorescent line energy (6.4 keV) than a power law spectrum of $\Gamma \sim 1.1$. EW is also proportional to metal abundance. The spectral fitting derives low metal abundance of ~0.2 solar, but the result is not likely to apply to the fluorescent line because the EW in Obs_{XMM1} exceeds the maximum EW (the case III when X-ray emission from a primary source is completely blocked and only fluorescent and scattering emission is observed). Circumstellar matter would be reasonably ~1 solar abundance and small metal abundance of the plasma should be made by another reason (see discussion in the latter paragraph). Assuming solar metal abundance, the best-fit EWs require partial covering of the direct X-ray emission by huge covering factor (~60%) for Obs_{XMM1} and small covering factor (~3%) for Obs_{XMM2}. Intrinsic X-ray luminosity in Obs_{XMM1} is then estimated to be log L_X ~31.2 ergs s^{-1}, which is comparable to L_X in Obs_{XMM2}.

A consistent explanation for the characteristics described in above two paragraphs is that a brightest active spot was behind the proto-stellar core in Obs_{XMM1} and just appeared from behind the rim in Obs_{XMM2} as a consequence of rotation of the proto-stellar core (Figure 7). Certainly, in the case of a solar hot spot, X-ray intensity roughly increases linearly during an appearance from the rim (e.g. top panel of Figure 3 of Sterling 1999), and a proto-stellar core can be regarded as an optically thick absorber. To be consistent with the observed time variation, the active spot should be confined in a small portion on the proto-stellar surface (probably within a quadrant) and rotate with a period $\gtrsim$2.8 days. Such an X-ray luminous small spot cannot be produced by solar type dynamo, and probably produced through mass accretion (see Bouvier 1990). The required rotational period is much slower than the break-up rotation, speculated for Class 0 protostars from rotational periods of Class I protostars (e.g. Montmerle et al. 2000).

The above picture also suggests that the intrinsic X-ray activity was constant between Obs_{XMM1} and Obs_{XMM2}, i.e. X_E^{XMM} was in a quiescent phase. The plasma temperature (kT

$\sim$3$-$4 keV) and X-ray luminosity (log $L_{\rm X} \sim 31.2$ ergs s^{-1}) far exceed the typical quiescent X-ray activity of Class I protostars, and are comparable to X-ray flares of Class I protostars (Imanishi et al. 2001; Shibata & Yokoyama 2002)[5]. This means that youngest protostars can continuously produce violent X-ray activity equivalent to flares from Class I protostars. Hot plasma temperature requires some acceleration mechanism, perhaps magnetic reconnection, in addition to gravitational mass infall. ($v_{ff} \sim$600 km s^{-1} of a $1M_\odot$ star can only produce plasma with $kT \sim$0.7 keV.) Montmerle et al. (2000) proposed a reconnection of large scale magnetosphere by core-disk differential rotation to explain periodic X-ray flares observed on the Class I protostar YLW15. A similar mechanism might be applicable to X_E^{XMM} though magnetic reconnection has to occur continuously to produce constant X-ray emission. The model predicts a jet (or outflow) production through the reconnection process (Hayashi et al. 1996). Interestingly, Class 0 protostars has an order of magnitude stronger CO outflow activity than Class I protostars (Bontemps et al. 1996), which is coincident with the X-ray luminosity ratio of X_E^{XMM} against typical Class I protostars.

Our thin-thermal model fit requires a metal abundance of $\sim$0.2 solar, which is mainly determined from intensity of the He-like iron line, but the strong fluorescent iron line suggests a near solar abundance in the surrounding cold gas. X-rays from pre-main-sequence stars show a similar problem regarding small coronal abundance (e.g., Favata et al. 2003). A possible solution is that the abundance anomaly localizes around the proto-stellar core. A well known phenomenon as such has a relation with first ionization potential (FIP) of element, so called the FIP effect. Unfortunately, we can not test the effect on X_E^{XMM} because abundance of high FIP elements such as argon ($0.1 \lesssim [Z/Z_\odot]_{Ar} \lesssim 12$ for Model C varying argon abundance) or neon (unmeasurable) is not well restricted against iron, a low FIP element. Another solution is that the continuum emission includes a non-thermal component, as is proposed for ρ Oph S1 (Hamaguchi et al. 2003).

If the dips in the light curves are really periodic, a possible geometry is that the X-ray hot spot confined on the proto-stellar core is blocked by an optically thick gas blob orbiting around the core. Orbital radius (r) of the Kepler rotation with rotational period of $\sim$13.9 ksec is $r = 1.2R_\odot \times (M/M_\odot)^{1/3}$ ($R_\odot$: solar radius, M: mass of the proto-stellar core). This means that a gas blob rotates very close to the stellar surface if it is a solar mass main-sequence star. Proto-stellar cores are thought to have several solar radius, and hence the derived orbit would be improbable. The dip feature is a riddle.

---

[5]We should note that Imanishi et al. (2001) use the distance to the ρ Oph cloud of 165 pc instead of 120 pc derived from more reliable *HIPPARCOS* data (Knude & Hϕg 1998) for a comparison to earlier X-ray results. The X-ray luminosity should be divided by a factor of two to compare our result.

6.2. What are X_E^{CXO} and X_W?

X_E^{CXO} has the radio counterpart 10E, but it does not have any IR counterpart ($K \gtrsim 19.4^m$) though the moderate N_H ($\sim 4\times10^{22}$ cm^{-2}) is typical of Class I protostars (generally, $K \lesssim 11^m$ in the field). The X-ray and radio emission is steady on short and long timescales (within a factor of three change between a day and 2.5 years in X-rays and $\lesssim$15% change in three observations between 1985–1998 in the centimeter radio wavelength, Brown 1987; Feigelson et al. 1998; Harju et al. 2001). Its radio spectral energy distribution combined with a marginal millimeter detection is consistent with free-free emission (Choi & Tatematsu 2004). These results agree with plasma, heated by a collision of a steady jet or outflow with circumstellar gas (Tsujimoto et al. 2004). Though X-ray plasma model derived in this paper has large uncertainty, log L_X $\sim$29.3–6 ergs s^{-1} is comparable to earliest detections of such emission in HH2 and L1551 IRS 5 (Pravdo et al. 2001; Favata et al. 2003), while plasma temperature >4 keV is much higher than those in HH2 and L1551 IRS 5 (T $\approx 10^6$ K) and comparable to TKH 8 in the OMC 2/3 cloud (Tsujimoto et al. 2004). Such plasma temperature requires an energetic jet with $v \gtrsim$1500 km s^{-1}, which has not been recognized in young stars so far. An alternative model with lower kT, higher N_H and larger L_X might be more reasonable (for example, kT $\sim$1.5 keV, N_H $\sim$ 1.4×10^{23} cm^{-2} and log L_X $\sim$30.3 ergs s^{-1}, which are acceptable to the X_E^{CXO} spectrum though it still needs $v \gtrsim$900 km s^{-1} and L_X comparable to stellar origin). On the other hand, the X-ray emission does not show any spatially extended feature, suggesting that the X-ray emitting (perhaps bow shock) region should be confined smaller than 1″ ($\sim$170 AU). If this hypothesis is correct, X_E^{XMM} ($\sim$340AU projected distance) is the closest and therefore the most plausible jet driving source. The jet would flow to the south-east direction, probably aligned with the rotational axis of X_E^{XMM} (Figure 7). We should note that Class 0 protostars drive larger momentum CO outflows than Class I protostars (Bontemps et al. 1996), and therefore would produce hotter plasma at the jet colliding region.

X_W has a bright near-IR counterpart IRS 7 as well as the centimeter radio counterpart 10W, and therefore might be a stellar origin. The N_H $\sim$2–6×10^{23} cm^{-2} is comparable to X_E^{XMM}, while the K-band magnitude ($\sim 12.2^m$) is comparable to Class I protostars in the field. X_W (IRS 7) might be a Class I source with a large inclination angle. On the other hand, the *ASCA* hard X-ray source exhibiting a strong X-ray flare in 1994 (Koyama et al. 1996) has been suspected to be IRS 7, but IRS 7 (X_W) has an order of magnitude larger N_H than the *ASCA* source (N_H $\sim 4.3\times10^{22}$cm^{-2}), and hence would not be the counterpart.

7. Summary & Conclusion

We discovered three extremely embedded X-ray sources in the IRS 7 core in the *XMM-Newton* and *Chandra* observations. In particular, X_E^{XMM} has not been recognized at any wavelengths, which means that X-ray observations can be a powerful tool to search for young protostars. Thanks to its vicinity to the Sun (d ~170 pc), the large effective area of *XMM-Newton* and a rare opportunity to catch an active state, we could obtain around ~2,000 photons from the young protostar X_E^{XMM}, which is around 40 times better than those obtained from X-ray emitting Class 0 candidates so far. The upperlimit to the K-band luminosity was restricted to ~1/150 of the OMC 2/3 protostars (d ~450 pc and completeness limit ~16^m, Tsujimoto et al. 2003). X_E^{XMM} would thus represent the most reliable X-ray detection of an example for the youngest protostars, and the best characterized in both IR and X-ray properties so far. The multiple X-ray observations and excellent photon statistics obtained with *XMM-Newton* enabled us to study the X-ray emission mechanism in further detail. The X-ray activity might be driven by strong mass accretion in the earliest phase of stellar evolution. The activity scale (kT ~3–4 keV, log L_X ~31 ergs s^{-1}) was actually far stronger than constant X-ray activity of Class I protostars, which would probably connect to the strong CO outflow phenomena seen around Class 0 protostars. The apparent time variability observed during the *XMM-Newton* observations could be produced by slow rotation of the proto-stellar core with a period of $\gtrsim$2.8 days. The period is much slower than the break-up rotation, speculated for Class 0 protostars from rotational periods of Class I protostars (e.g. Montmerle et al. 2000). This may mean that angular momentum is effectively removed from accreting gas during the mass accretion process. The weak metal abundance feature of ~0.2 solar was also seen in young protostars. This suggests that local abundance anomaly around the proto-stellar core can develop within ~10^4 years or the feature is apparently made by fundamental X-ray emission mechanism such as non-thermal process. On the other hand, X_E^{CXO} has some characteristics of a jet induced plasma. X_E^{XMM} and X_E^{CXO} might form an X-ray jet driving and induced system.

The evolutionary status of X_E^{XMM} as whether a Class 0 protostar or an intermediate phase between Class 0 and I protostars should be elucidated by constructing the IR and radio SED. For the purpose, we need high spatial resolution and sensitive observations in IR and radio wavelengths. Ground based 10m class , Spitzer and ALMA telescopes will be good instruments to reveal the nature of this mysterious X-ray protostar. Detection of a jet feature and measurement of the jet direction would help to know the inclination of the rotational axis as well. On the other hand, revisit of the field with X-ray observatories with a long exposure could detect periodical X-ray time variation of X_E^{XMM} by the core rotation, restrict plasma nature of X_E^{CXO} and X_W with better photon statistics, and discover other X-ray emitting young protostars, which would be hidden inside gas clumps in the field.

We are grateful to M. Tsujimoto, Y. Tsuboi, K. Koyama, K. Tatematsu, M. Choi, T. Yokoyama, S. Yashiro, S. Morita for useful comments. This work is performed while K.H. held awards by National Research Council Research Associateship Award at NASA/GSFC, and supported by *XMM-Newton* US grant.

Facilities: XMM-Newton(EPIC), CXO(ACIS-I). UH88(QUIRC)

REFERENCES

Anderson, I. M., Harju, J., Knee, L. B. G., & Haikala, L. K. 1997, A&A, 321, 575

Andre, P., Ward-Thompson, D., & Barsony, M. 1993, ApJ, 406, 122

Aschenbach, B., Briel, U. G., Haberl, F., Braeuninger, H. W., Burkert, W., Oppitz, A., Gondoin, P., & Lumb, D. H. 2000, in Proc. SPIE Vol. 4012, p. 731-739, X-Ray Optics, Instruments, and Missions III, Joachim E. Truemper; Bernd Aschenbach; Eds., 731–739

Bontemps, S., Andre, P., Terebey, S., & Cabrit, S. 1996, A&A, 311, 858

Bouvier, J. 1990, AJ, 99, 946

Brown, A. 1987, ApJ, 322, L31

Chini, R., Kämpgen, K., Reipurth, B., Albrecht, M., Kreysa, E., Lemke, R., Nielbock, M., Reichertz, L. A., Sievers, A., & Zylka, R. 2003, A&A, 409, 235

Choi, M., & Tatematsu, K. 2004, ApJ, 600, L55

Favata, F., Giardino, G., Micela, G., Sciortino, S., & Damiani, F. 2003, A&A, 403, 187

Feigelson, E. D., Carkner, L., & Wilking, B. A. 1998, ApJ, 494, L215+

Garmire, G., & Garmire, A. 2002, APS Meeting Abstracts, 17064

Grosso, N., Montmerle, T., Feigelson, E. D., Andre, P., Casanova, S., & Gregorio-Hetem, J. 1997, Nature, 387, 56

Güdel, M., Audard, M., Smith, K. W., Sres, A., Escoda, C., Wehrli, R., Guinan, E. F., Ribas, I., Beasley, A. J., Mewe, R., Raassen, A. J., Behar, E., & Magee, H. 2001, in Proceedings of the 12th Cambridge Workshop of Cool Stars, Stellar Systems, and the Sun: The Future of Cool-Star Astrophysics, ed. A. Brown, T. R. Ayres, & G. M. Harper, Boulder: Univ. of Colorado, in press

Hamaguchi, K., Corcoran, M. F., & Imanishi, K. 2003, PASJ, 55, 981

Harju, J., Haikala, L. K., Mattila, K., Mauersberger, R., Booth, R. S., & Nordh, H. L. 1993, A&A, 278, 569

Harju, J., Higdon, J. L., Lehtinen, K., & Juvela, M. 2001, in ASP Conf. Ser. 235: Science with the Atacama Large Millimeter Array, 125–+

Hayashi, M. R., Shibata, K., & Matsumoto, R. 1996, ApJ, 468, L37

Henning, T., Launhardt, R., Steinacker, J., & Thamm, E. 1994, A&A, 291, 546

Imanishi, K., Koyama, K., & Tsuboi, Y. 2001, ApJ, 557, 747

Inoue, H. 1985, Space Science Reviews, 40, 317

Jansen, F., Lumb, D., Altieri, B., Clavel, J., Ehle, M., Erd, C., Gabriel, C., Guainazzi, M., Gondoin, P., Much, R., Munoz, R., Santos, M., Schartel, N., Texier, D., & Vacanti, G. 2001, A&A, 365, L1

Kastner, J. H., Richmond, M., Grosso, N., Weintraub, D. A., Simon, T., Frank, A., Hamaguchi, K., Ozawa, H., & Henden, A. 2004, Nature, submitted

Knude, J., & Hϕg, E. 1998, A&A, 338, 897

Koyama, K., Hamaguchi, K., Ueno, S., Kobayashi, N., & Feigelson, E. D. 1996, PASJ, 48, L87

Kraft, R. P., Burrows, D. N., & Nousek, J. A. 1991, ApJ, 374, 344

Mewe, R., Kaastra, J. S., & Liedahl, D. A. 1995, Legacy, 6, 16

Montmerle, T., Grosso, N., Tsuboi, Y., & Koyama, K. 2000, ApJ, 532, 1097

Morrison, R., & McCammon, D. 1983, ApJ, 270, 119

Pravdo, S. H., Feigelson, E. D., Garmire, G., Maeda, Y., Tsuboi, Y., & Bally, J. 2001, Nature, 413, 708

Rho, J., Ramírez, S. V., Corcoran, M. F., Hamaguchi, K., & Lefloch, B. 2004, ApJ, submitted.

Saraceno, P., André, P., Ceccarelli, C., Griffin, M., & Molinari, S. 1996, A&A, 309, 827

Shibata, K., & Yokoyama, T. 2002, ApJ, 577, 422

Stelzer, B., Neuhäuser, R., & Hambaryan, V. 2000, A&A, 356, 949

Sterling, A. C. 1999, A&A, 346, 995

Strüder, L., Briel, U., Dennerl, K., Hartmann, R., Kendziorra, E., Meidinger, N., Pfeffermann, E., Reppin, C., Aschenbach, B., Bornemann, W., Bräuninger, H., Burkert, W., Elender, M., Freyberg, M., Haberl, F., Hartner, G., Heuschmann, F., Hippmann, H., Kastelic, E., Kemmer, S., Kettenring, G., Kink, W., Krause, N., Müller, S., Oppitz, A., Pietsch, W., Popp, M., Predehl, P., Read, A., Stephan, K. H., Stötter, D., Trümper, J., Holl, P., Kemmer, J., Soltau, H., Stötter, R., Weber, U., Weichert, U., von Zanthier, C., Carathanassis, D., Lutz, G., Richter, R. H., Solc, P., Böttcher, H., Kuster, M., Staubert, R., Abbey, A., Holland, A., Turner, M., Balasini, M., Bignami, G. F., La Palombara, N., Villa, G., Buttler, W., Gianini, F., Lainé, R., Lumb, D., & Dhez, P. 2001, A&A, 365, L18

Townsley, L. K., Broos, P. S., Garmire, G. P., & Nousek, J. A. 2000, ApJ, 534, L139

Tsuboi, Y., Imanishi, K., Koyama, K., Grosso, N., & Montmerle, T. 2000, ApJ, 532, 1089

Tsuboi, Y., Koyama, K., Hamaguchi, K., Tatematsu, K., Sekimoto, Y., Bally, J., & Reipurth, B. 2001, ApJ, 554, 734

Tsuboi, Y., Koyama, K., Murakami, H., Hayashi, M., Skinner, S., & Ueno, S. 1998, ApJ, 503, 894

Tsujimoto, M., Koyama, K., Kobayashi, N., Goto, M., Tsuboi, Y., & Tokunaga, A. T. 2003, AJ, 125, 1537

Tsujimoto, M., Koyama, K., Kobayashi, N., Saito, M., Tsuboi, Y., & Chandler, C. J. 2004, PASJ, in press

Turner, M. J. L., Abbey, A., Arnaud, M., Balasini, M., Barbera, M., Belsole, E., Bennie, P. J., Bernard, J. P., Bignami, G. F., Boer, M., Briel, U., Butler, I., Cara, C., Chabaud, C., Cole, R., Collura, A., Conte, M., Cros, A., Denby, M., Dhez, P., Di Coco, G., Dowson, J., Ferrando, P., Ghizzardi, S., Gianotti, F., Goodall, C. V., Gretton, L., Griffiths, R. G., Hainaut, O., Hochedez, J. F., Holland, A. D., Jourdain, E., Kendziorra, E., Lagostina, A., Laine, R., La Palombara, N., Lortholary, M., Lumb, D., Marty, P., Molendi, S., Pigot, C., Poindron, E., Pounds, K. A., Reeves, J. N., Reppin, C., Rothenflug, R., Salvetat, P., Sauvageot, J. L., Schmitt, D., Sembay, S., Short, A. D. T., Spragg, J., Stephen, J., Strüder, L., Tiengo, A., Trifoglio, M., Trümper, J., Vercellone, S., Vigroux, L., Villa, G., Ward, M. J., Whitehead, S., & Zonca, E. 2001, A&A, 365, L27

Ueda, Y., Takahashi, T., Inoue, H., Tsuru, T., Sakano, M., Ishisaki, Y., Ogasaka, Y., Makishima, K., Yamada, T., & Ohta, K. 1998, Nature, 391, 866

van den Ancker, M. E. 1999, PhD thesis, Universiteit van Amsterdam

Weisskopf, M. C., Brinkman, B., Canizares, C., Garmire, G., Murray, S., & Van Speybroeck, L. P. 2002, PASP, 114, 1

Wilking, B. A., McCaughrean, M. J., Burton, M. G., Giblin, T., Rayner, J. T., & Zinnecker, H. 1997, AJ, 114, 2029

Table 1. Observation Logs

Observation	Observatory	Seq. ID	Date	Exposure (ksec)	Δ_{axis}	Shift ($\Delta\alpha$,$\Delta\delta$)
Obs_{XMM1}	*XMM-Newton*	146390101	2003 Mar. 28	14.9/21.5	6′	(0.″ 4, −1.″ 0)
Obs_{XMM2}	*XMM-Newton*	146390201	2003 Mar. 29	18.1/24.0	6′	(0.″ 2, −1.″ 3)
Obs_{CXO}	*Chandra*	200017	2000 Oct. 7	19.7	2′	(0.″ 03, 0.″ 23)

Note. — Exposure: pn/MOS for *XMM-Newton*. Δ_{axis}: Off-axis angle of the IRS7 region. Objects used for the position correction: IRS2, IRS5, HBC677, CrA1, ISO-CrA136, HH101 IRS 4, ISO-CrA137, TY CrA and HD 176386. IRS1 and ISO-CrA134 were also used for the position correction of Obs_{CXO}.

Table 2. Detected Sources

Source	Abbr.	Observation	(α_{2000}, δ_{2000}) (h m s, d ′ ″)	Error[a]	Net cnts (cnts)	K-band (mag)	Counterpart
XMMU J190156.3-365726	X_E^{XMM}	Obs_{XMM1}	19 1 56.29, −36 57 26.5	1.″ 7	467.7	$\gtrsim$19.4	···
		Obs_{XMM2}	19 1 56.32, −36 57 26.4	1.″ 2	1611.3	···	···
XMMU J190155.3-365721	X_W^{XMM}, X_W	$Obs_{XMM1\&2}$	19 1 55.26, −36 57 20.8	∼3″	114.0[b]	12.2[c]	10W[d] , Source 4[e] , IRS7
CXOU J190156.4-365728	X_E^{CXO}	Obs_{CXO}	19 1 56.43, −36 57 27.7	1.″ 0	19.6	$\gtrsim$19.4	10E[d]
CXOU J190155.3-365722	X_W^{CXO}, X_W	Obs_{CXO}	19 1 55.34, −36 57 21.6	1.″ 0	12.7	12.2[c]	10W[d] , Source 4[e] , IRS7

Note. — Net cnts: EPIC pn + MOS for *XMM-Newton*.

[a]90% confidence error.

[b]Net counts in Obs_{XMM1}.

[c]Reference of the K′ magnitude of R1 (IRS7) to Wilking et al. (1997).

[d]Reference to Brown (1987) and Feigelson et al. (1998).

[e]Reference to Choi & Tatematsu (2004).

Table 3. Fitting Result of the X_E^{XMM} Light Curves

Observation	Binning (sec)	Model	Constant (10^{-2} cnts s^{-1})	Linear (10^{-2} cnts s^{-1} day^{-1})	χ^2/d.o.f. (d.o.f.)
Obs_{XMM1}	2,000	con.	0.93	···	1.63 (13)
Obs_{XMM2}	1,000	con.	5.3	···	1.96 (26)
	1,000	con.+lin.	3.7[a]	9.3	1.21 (25)

[a]Count rate at TJD = 12727.8564 day.

Note. — con.: constant, lin.: linear

Table 4. Fitting Results of the Spectra

Source	Observation	Model	Comp.	$N_{\rm H}$ (10^{22}cm^{-2})	kT (keV)	Abundance (solar)	log $E.M.$ (cm^{-3})	Flux$_{0.4keV}$ (10^{-6} cnts cm^{-2} s^{-1})	χ^2/d.o.f. (d.o.f)	log $L_{\rm X}$ (ergs s^{-1})
$X_{\rm E}^{\rm XMM}$	Obs$_{\rm XMM1}$	A(1T)		13.2 (9.6−18.3)	5.1 (2.8−10.4)	0.5 (0.2−1.4)	53.2 (53.0−53.6)	2.4	1.22 (21)	30.4
	Obs$_{\rm XMM2}$	B(1T)		24.7 (21.6−28.3)	4.4 (3.4−6.1)	0.2 (0.1−0.3)	54.1 (54.0−54.1)	3.4	0.99 (66)	31.2
	Obs$_{\rm XMM1\&2}$	C(2T)	Var$_1$	28.1 (22.5−33.8)	2.7 (1.8−4.2)	0.2 (0.1−0.3)	53.8 (53.5−54.1)	2.8 (0.8−4.8)	0.97 (86)	30.8
			Var$_2$	=Var$_1$	4.0 (2.9−5.3)	=Var$_1$	54.1 (54.0−54.4)	3.4 (1.4−5.5)	···	31.2
			Const.	4.2 (1.4−11.4)	2.3 (0.4−)	=Var$_1$	52.5 (51.8−53.5)	···	···	29.6
$X_{\rm E}^{\rm CXO}$	Obs$_{\rm CXO}$	D(1T)		4.2 (fix)	> 4.3	0.3 (fix)	52.1 (51.8−52.2)	···	1.36 (2)	29.3
$X_{\rm W}^{\rm XMM}$	Obs$_{\rm XMM1}$	E(1T)		33.7 (19.1−60.0)	4.7 (1.6−)	0.3 (fix)	53.3 (52.8−54.3)	···	0.65 (8)	30.5
$X_{\rm W}^{\rm CXO}$	Obs$_{\rm CXO}$	F(1T)		33.7 (fix)	4.7 (fix)	0.3 (fix)	52.8 (52.6−53.0)	···	0.01 (3)	30.0

Note. — Var$_{1(2)}$: variable component in Obs$_{\rm XMM1}$ (Obs$_{\rm XMM2}$). Const.: constant (soft) component of the Obs$_{\rm XMM1}$ and Obs$_{\rm XMM2}$ spectra. $L_{\rm X}$: luminosity in the 0.5−10 keV band. Distance assumes $d \sim$170 pc.

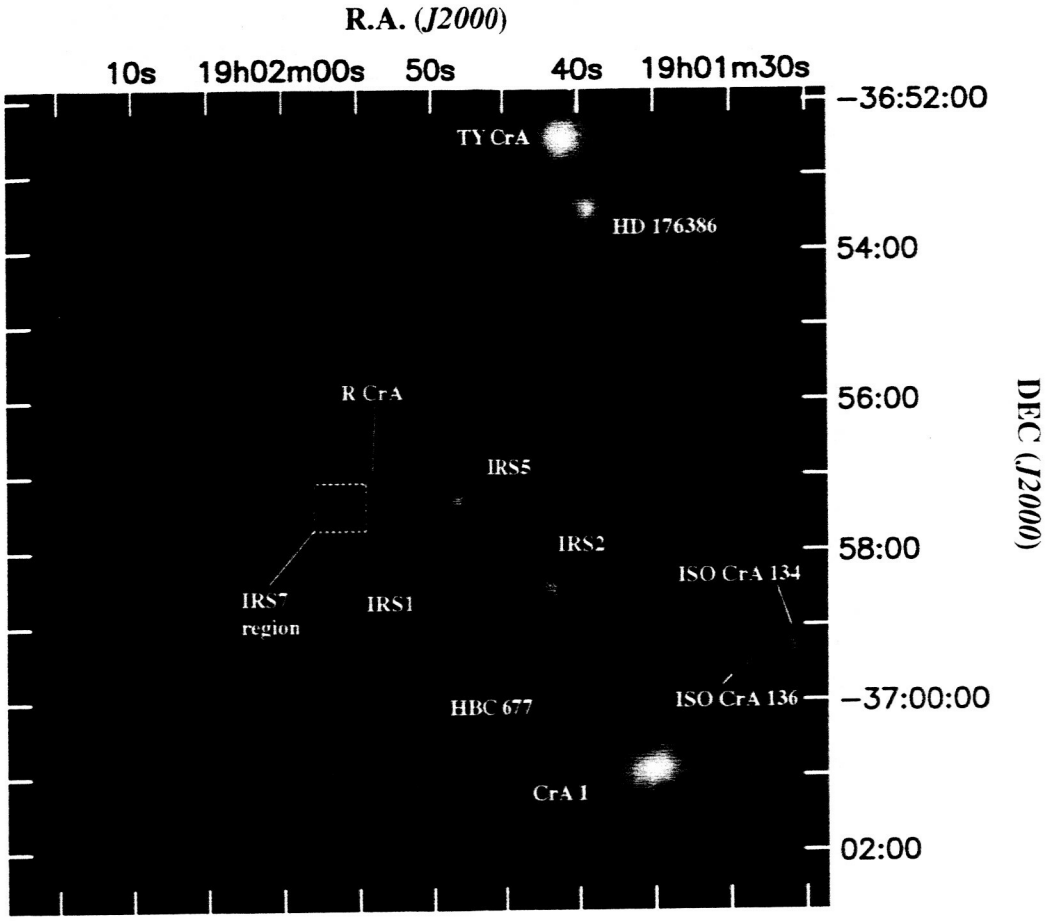

Fig. 1.— *XMM-Newton* true color image of the R CrA star forming region (Obs_{XMM1} + Obs_{XMM2}). The image is color coded to represent hard band (3–9 keV) to blue, medium band (1–3 keV) to green and soft band (0.2–1 keV) to red. The dotted square shows the IRS 7 region (field of view of the top panels of Figure 2). Class I protostar: IRS 1, IRS 2 and IRS 5, Herbig Ae/Be star: R CrA, TY CrA, HD 176386, Weak-lined T-Tauri star: CrA 1.

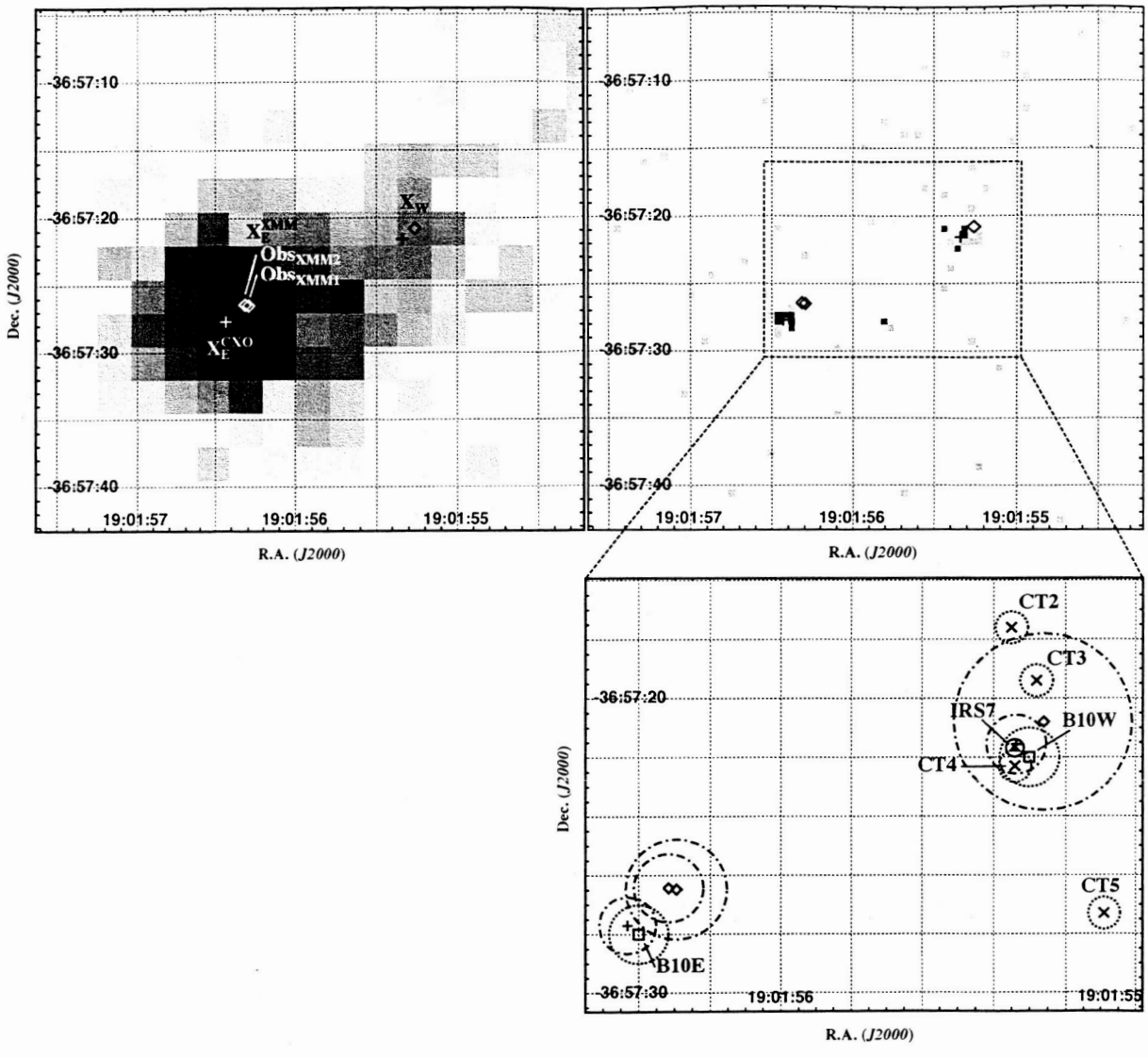

Fig. 2.— Magnified images of the IRS 7 region. The top left panel shows the 3−9 keV EPIC pn + MOS image of *XMM-Newton* (Obs_{XMM1} + Obs_{XMM2}), the top right panel shows the 0.5−9 keV image of *Chandra* (Obs_{CXO}) and the bottom right panel shows source positions with their error circles including sources in near-IR and radio wavelengths. Diamonds show *XMM-Newton* sources, crosses *Chandra* sources, squares centimeter radio sources (B*number*, Brown 1987, Source positions are referred to Feigelson et al. 1998), x millimeter radio sources (CT*number*, Choi & Tatematsu 2004), a triangle near-IR source (IRS 7). Error circles are shown in dot-bar line for X-ray sources and dotted line for radio sources and solid line for near-IR source. Error circles of X-ray sources for the 2MASS frame is smaller than the above, and those of X_E^{XMM} (Obs_{XMM2}) and X_E^{CXO} do not overlap with each other.

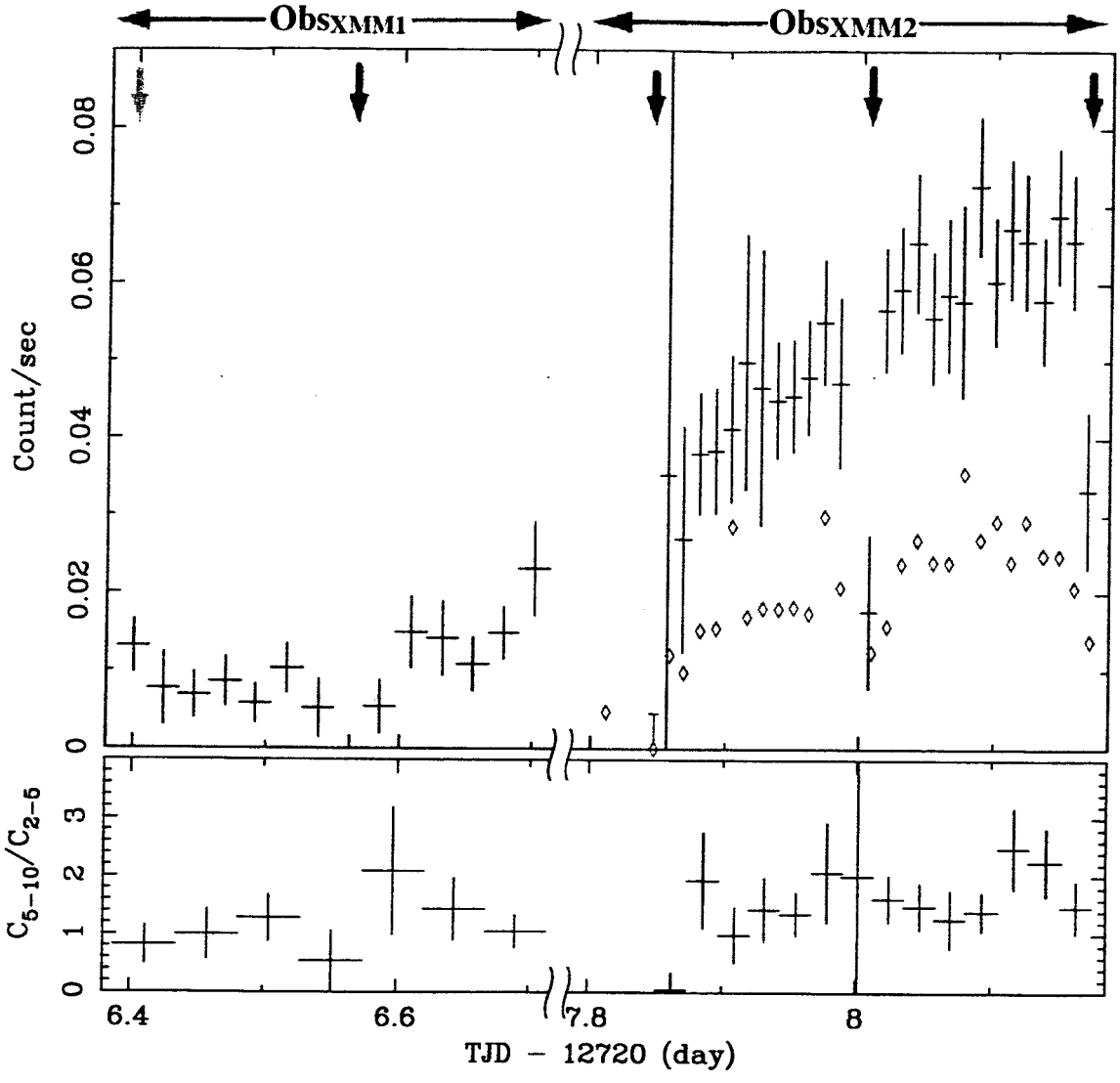

Fig. 3.— Light curves of X_E^{XMM} in the 2–10 keV band (*top panel*) and the hardness ratio defined as "count rates in the 5–10 keV band / count rates in the 2–5 keV band" (*bottom panel*). Points with error bars in the top and bottom panel are made from summed data sets of pn plus MOS, while grey diamonds and an error bar at 7.85 day in Obs_{XMM2} show light curves of MOS (1+2). The horizontal axis is truncated Julian day (TJD) – 12720. The black arrows show timing of the dip feature and the grey arrow does a possible dip timing assuming the period of 13.9 ksec. Bins in the top panel have 2 ksec (Obs_{XMM1}) and 1 ksec (Obs_{XMM2}), and bins in the bottom panel have 4 ksec (Obs_{XMM1}) and 2 ksec (Obs_{XMM2}).

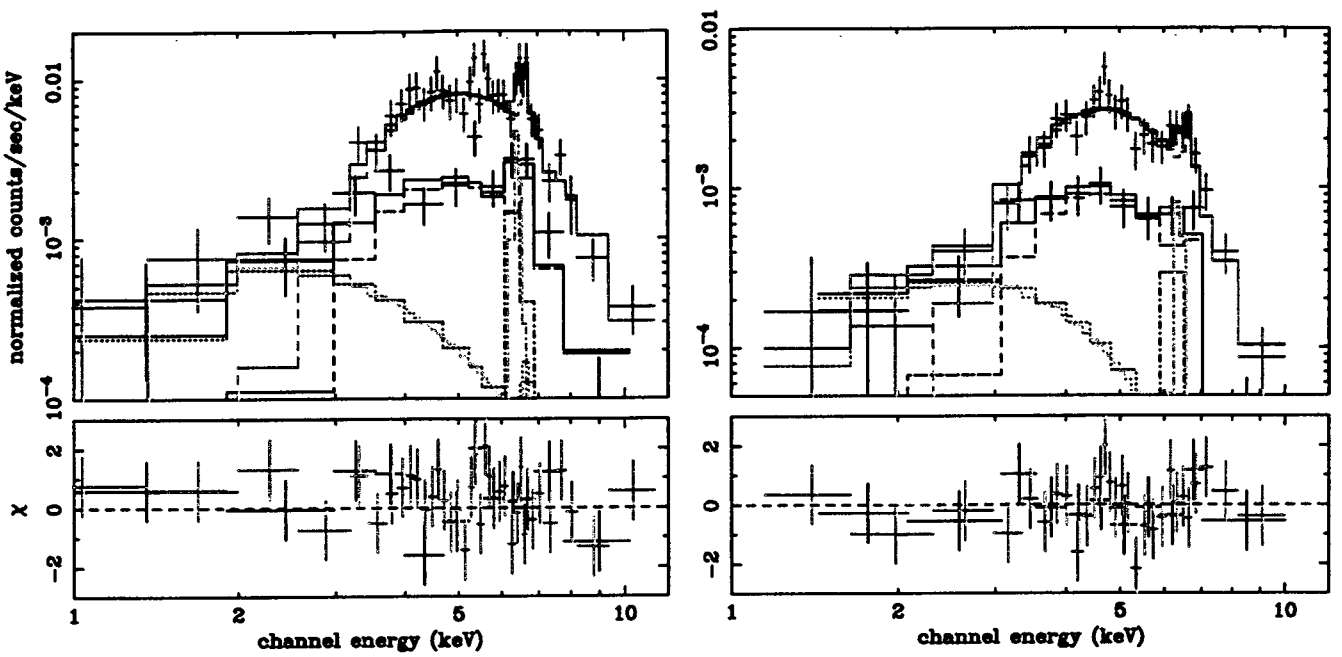

Fig. 4.— EPIC pn (*left*) and MOS1+2 (*right*) spectra of X_E^{XMM} in Obs_{XMM1} (*black*) and Obs_{XMM2} (*red*). Solid lines show the best-fit model of the simultaneous fitting with EPIC pn and MOS. Dotted lines show the constant (soft) component, barred line the variable components, and dot-bar lines the Gaussian component. The bottom panel shows residual of the χ^2 fit.

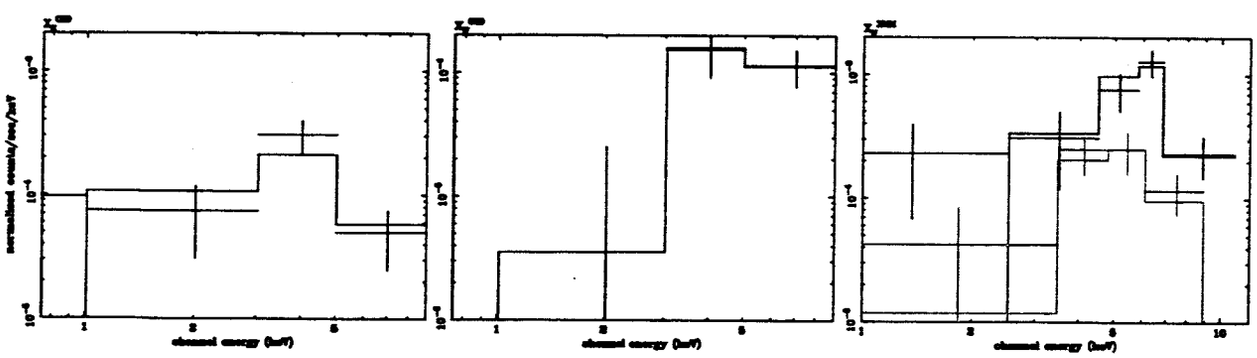

Fig. 5.— *Chandra* spectra of X_E^{CXO} (*left*) and X_W (*center*), and *XMM-Newton* spectra of X_W in Obs_{XMM1} (*right*, black–pn, red–MOS). Solid lines show the best-fit models (Model D, F and E in Table 4 from left).

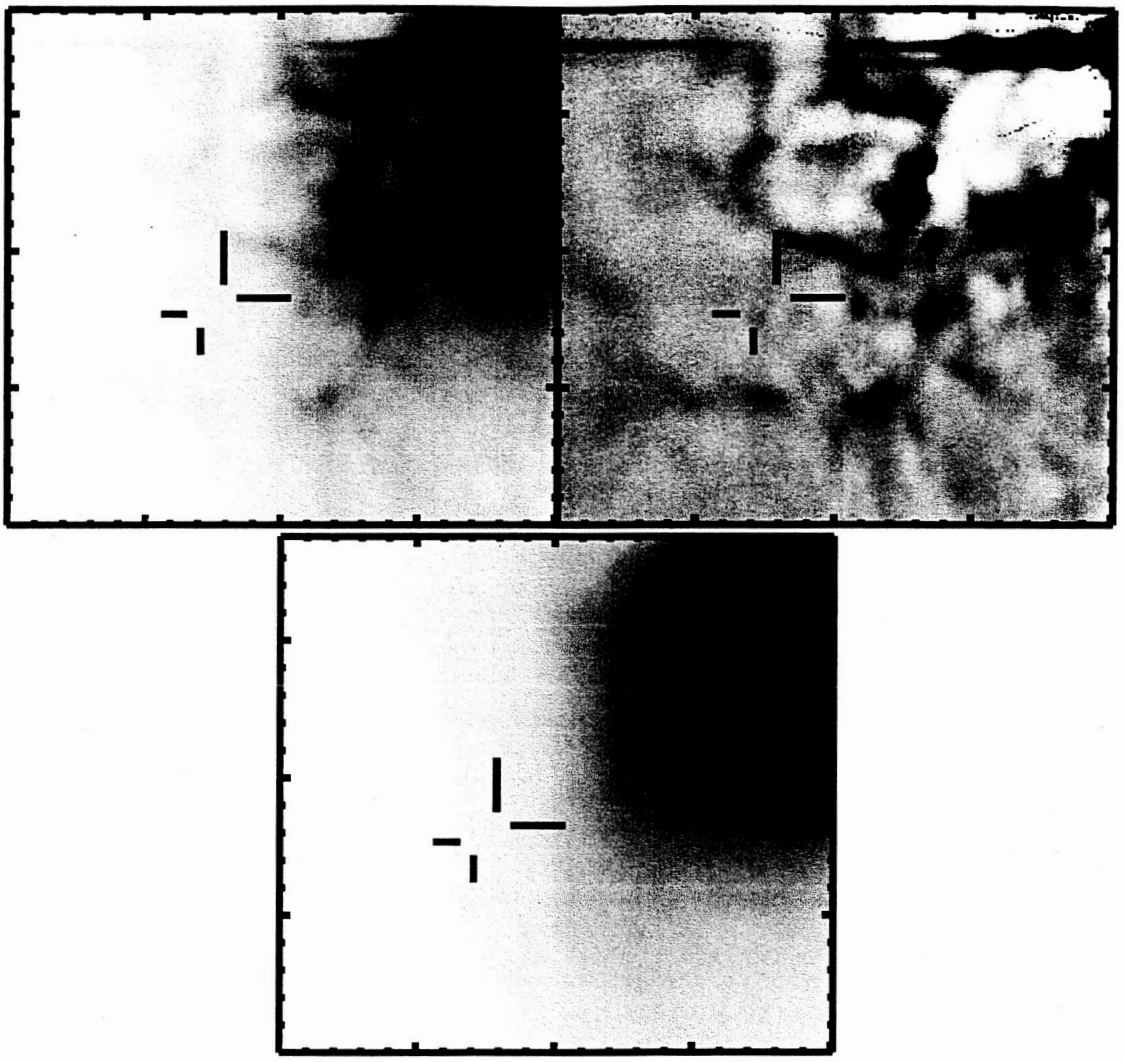

Fig. 6.— The K-band image of the IRS7 region obtained in 1998 (*top left*: original image, *bottom*: fit of the original image by the median-filtering method, *top right*: subtracted image). X_E^{XMM} are at the cross of two long (horizontal and vertical) bars. X_E^{CXO} (*left*) and X_W^{CXO} (X_W, *right*) are at the crosses of short bars.

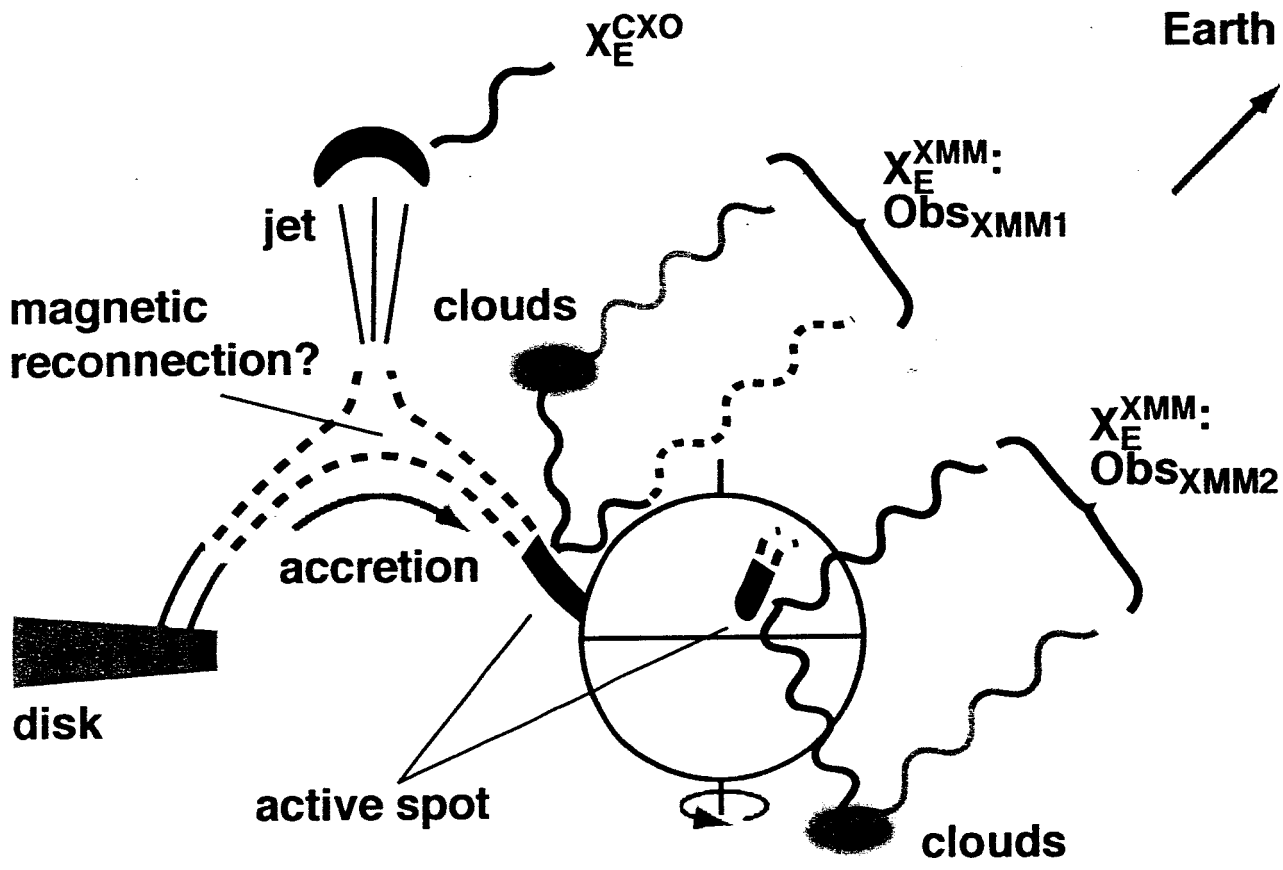

Fig. 7.— A possible geometry of the proto-stellar core, jet and observer . The wavy lines show X-ray emission (solid black: direct X-rays, gray: fluorescent and scattering X-rays, dotted black: direct X-rays are partially covered).